DEVELOPMENT OF A TWO-DIMENSIONAL AXIAL SYMMETRY MODEL FOR WIRE ARC ADDITIVE MANUFACTURING

S. CADIOU*, M. COURTOIS*, M. CARIN*, P. LE MASSON*, L. GUILMOIS**'*** and P. PAILLARD**

*Univ. Bretagne Sud, UMR CNRS 6027, IRDL, F-56100 Lorient, France, e-mail: Stephen.cadiou@univ-ubs.fr
**Polytech Nantes, UMR 6502, IMN F-44000 Nantes, France
***IRT Jules Verne, Chemin du Chaffault, F-44340 Bouguenais, France

DOI 10.3217/978-3-85125-615-4-56

ABSTRACT

In this study, a numerical model taking into account electromagnetism, fluid flow, and heat transfer in the arc and the melt pool is developed using COMSOL Multiphysics®. The level set method is used to simulate the layer-by-layer addition of materials along the vertical axis to form a cylindrical rod. This shape has the advantage to be simulated with a 2D axial-symmetry model in order to reduce computation time. The implementation of the arc plasma model is first validated by comparing predictions with literature data. Then, the arc pressure, arc shear stress, Lorentz forces and heat flux are analysed and used to define source terms for the additive manufacturing model. In this model, the building of a 308 stainless steel rod is simulated by adding molten metal droplet along the vertical axis. The adding of droplets and heat source are periodically stopped in order to simulate the layer-by-layer build-up of the rod. The calculated shape and the temperature field are analysed and compared to experimental data.

Keywords: Modeling, Multiphysics, Additive Manufacturing, WAAM

INTRODUCTION

The additive manufacturing (AM) of metal parts is a revolutionary process with great potential. A large number of additive manufacturing methods are now available. The current work focuses on the Wire Arc Additive Manufacturing (WAAM), which is a highly promising process due to its high deposition rate and efficiency (100%). This process uses an electric arc as a heat source and a wire as feedstock and is very similar to the GMA (Gas Metal Arc) welding process. However, a thorough understanding of the physical phenomena involved in WAAM is desirable to produce defect-free and reliable AM parts. Numerical simulation provides an efficient way to understand the influence of the operating parameters on the geometry, the thermal cycles, the microstructure, the distortions and the residual stresses observed in the AM parts.

In the literature, there are different models concerning the numerical simulation of arc welding and additive arc wire fabrication. The most complete models are those dealing with the physical phenomena in the arc. Many authors have proposed arc model without filler material to simulate Tungsten Inert Gas (TIG) welding process (Hsu [1], Tanaka [2] [3] [4], Brochard [5], Traidia [6], Lago [7], Li [8], Yau [9]). These models have the advantage of describing the main physical phenomena only from the operating parameters and material properties and can be regarded as self-consistent models. In parallel, models simulating Gas Metal Arc Welding (GMAW) and Wire Arc Additive Manufacturing (WAAM) were developed. Murphy [10] and Luo [11] have developed models focusing on the evolution of the droplet in the arc. Fan [12], Hu [13], [14] have developed models able to track the formation as well as the detachment of droplets from the wire electrode, and its transfer through the arc and into the weld pool. In these studies, a stationary two-dimensional axisymmetric GMAW system is considered. The Volume of Fluid (VOF) method is employed for tracking the free surface of the droplets and the melt pool. With this method, the mass conservation is well satisfied, but the interface reconstruction is quite difficult and the implementation in 3D is tedious and time consuming [15]. It is also possible to use a level set method to track the gas-metal interface. Desmaison [16] used this method to simulate in 3D the material supply at the melt pool surface during a laser/GMAW welding process. However, there are very limited numerical studies in 3D to simulate multilayer deposition such as in WAAM processes, since a complete 3D modeling has to face prohibitive calculation times. In order to reduce calculation times, these models are generally simplified and based on empirical laws requiring a calibration of input parameters with experimental data. The droplet formation and detachment, droplet flight in arc plasma and impingement of droplets are not explicitly simulated. Bai [17] developed a 3D model to investigate the fluid flow and heat transfer behaviours in multilayer deposition of plasma arc welding (PAW). A VOF method is used to track the melt pool surface. The mass feeding process is modelled as a source term in the mass conservation equation. The location of the mass input is determined according to experimental data. The heat of arc is also simplified using a modified double-ellipsoidal volumetric heat source model based on calibrated parameters with IR imaging. This model is used to simulate the 1^{st}, 2^{nd} and 21^{st} layer depositions. However, due to prohibitive computation time, the simulation of the 21^{st} layer is initialized with the experimental profile of the 20^{th} layer. Hejripour [18] used an Arbitary Lagrangian-Eulerian (ALE) method to predict the shape of the first layer in a WAAM process. Gaussian functions are chosen to describe the heat input, the current density and the arc pressure. The profile of the free surface is calculated by minimizing the total potential energy of the surface resulting from a balance condition between surface tension, hydrostatic pressure and arc pressure. However, this method is difficult to apply for multilayer deposition. Note that in all these studies, in order to validate the models, the comparisons are limited to the shape of geometry and to macrographs for fusion zone.

In this paper, a two-dimensional axial-symmetric model taking into account electromagnetism, fluid flow, and heat transfer in the arc and the melt pool is first presented. This arc model is used to define the heat input of a WAAM model. A level set method is used for simulating the layer-by-layer addition of materials along the vertical axis. In this model, the manufacturing of a 308 stainless steel rod by a WAAM process is simulated.

The calculated shape and the temperature field are analysed and compared to experimental data.

MODELING OF ARC WELDING

In order to determine the heat input induced by the arc based solely on the operating parameters, an arc model is developed in the case of tungsten cathode. Many physical phenomena have to be considered in the arc and the melt pool as shown in Fig. 1.

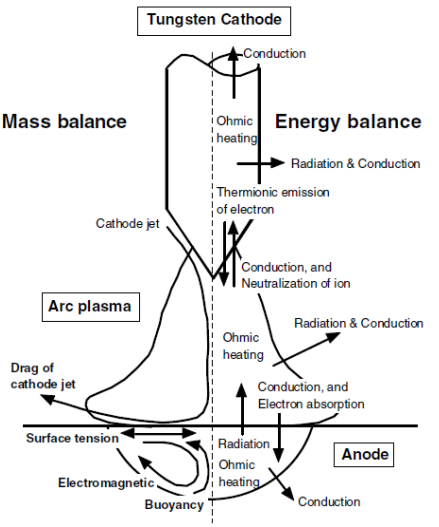

Fig.1 Main physical phenomena taken into account in the numerical modeling of arc welding [2].

THE COMPUTATIONAL MODEL

The mathematical modeling of such a process involves different physics like heat transfer, fluid flow, or electromagnetism. The present model is focused on these three physics, which is also refer to a Magneto-Hydro Dynamics (MHD) model. The aim of this approach is to predict the heat transfer and fluid flow in both the arc plasma and the weld pool. This model is based on that of Hsu [1] and Tanaka [2] [3] [4]. Their works have been used as references for many researchers [5-8] in order to validate MHD models of arc welding.

Based on these reference cases, the following assumptions are considered:

- The model is solved in 2D axisymmetric, since the TIG torch is static,
- The plasma is in local thermodynamic equilibrium (LTE). This assumption means that species such as ions, neutrons are supposed to have the same temperature. However this assumption is not valid near cathode / plasma interface and anode / plasma interface. To overcome this, conditions are applied to these interfaces as done in [2-8]. Moreover, Haidar [19] showed that the plasma is in LTE, if arc

length is superior to 2 mm and the temperature reaches 12 000 K. This is the case with our model.
- The fluid flow in the plasma is considered to be Newtonian laminar with a weakly compressible approach,
- A Newtonian laminar incompressible flow is considered in the melt pool,
- The cathode and anode are not considered deformable. Traidia showed that for low current welding (up to 180 A) the free surface depression is negligible [6]. To reduce computational time, the anode is not deformable.
- Buoyancy force is taken into account using the Boussinesq approximation.
- The effect of metal vapours coming from the vaporisation of the melt pool surface on the transport properties of the arc is not included in the model.

When the arc interacts with the anode, metal vapor can be generated if the surface temperature reaches the evaporation point. Several studies have been carried out on the understanding of the influence of these metallic vapors. Lago, [7], shows through his numerical model that metal vapors tend to cool the plasma essentially at the edges. Current densities, in the presence of metal vapors, increase at the center of the arc and decrease at the edges. Moreover, the vapors increase the current densities at the anode. The greater flux comes from the increase of the electrical flux due to the electrical conductivities increase. These remarks are consistent with Mougenot [20]. Murphy and Tanaka et al [21] have shown that the maximum value of the current density is slightly lower (5.5% difference) when the metal vapors are taken into account. In our case, we chose to neglect the metallic vapors since their effect is rather small but also in order to simplify the calculations.

With these assumptions, the governing equations of heat and mass transfer for arc and metal transport are given below:

- Conservation of mass

$$\frac{\partial \rho}{\partial t} + div(\rho \vec{v}) = 0 \tag{1}$$

where ρ is the density, t the time and $\vec{v}$ the velocity vector.

- Conservation of momentum

$$\rho\left(\frac{\partial \vec{v}}{\partial t} + \overline{\overline{grad}}(\vec{v}).\vec{v}\right) = \overrightarrow{div}\left[-P\bar{\bar{\imath}} + \mu_f\left(\overline{\overline{grad}}(\vec{v}) + {}^t\overline{\overline{grad}}(\vec{v})\right) - \frac{2}{3}div(\vec{v})\bar{\bar{\imath}}\right] + \overrightarrow{F_v} \tag{2}$$

where P is the pressure, $\bar{\bar{\imath}}$ the identity matrix, μ_f the dynamic viscosity and $\overrightarrow{F_v}$ the volume force detailed below.

In the plasma, this volume force is an electromagnetic force:

$$\vec{F_v} = \vec{F}_{mag} = \vec{j} \times \vec{B} \tag{3}$$

where B is the magnetic flux density and j is the current density.
In the melt pool, the volume force is expressed as follows:

$$\vec{F}_v = \vec{F}_{mag} + \vec{F}_b + \vec{F}_{Darcy} = \vec{j} \times \vec{B} - \rho_{ref}\beta\left(T - T_{ref}\right)\vec{g} - C\frac{(1-f_L)^2}{f_L^3 + b}\vec{v} \quad (4)$$

where $\vec{F}_b$ is the buoyancy force, $\vec{F}_{Darcy}$ is the Darcy law. The Darcy law enables to stop the fluid flow in the solid region. ρ_{ref} is the density at the reference temperature T_{ref}, β is the thermal expansion coefficient, $\vec{g}$ is the acceleration due to gravity, C is a relatively huge constant that ensures the decrease of the velocity field in the solid region, b is a relatively low constant introduced to avoid division by zero and f_L is the liquid fraction function. This function is assumed to vary linearly with temperature in the mushy zone as follows:

$$f_L = \begin{cases} 1 & \text{if } T > T_L \\ \frac{T - T_S}{T_L - T_S} & \text{if } T_S \leq T \leq T_L \\ 0 & \text{if } T < T_S \end{cases} \quad (5)$$

where T is the temperature, T_S and T_L are the solidus and liquidus temperatures of the workpiece material.

- Conservation of energy

$$\rho C_p^{eq}\left(\frac{\partial T}{\partial t} + \vec{v}.\overrightarrow{grad}(T)\right) = div\left(\bar{\bar{k}}\,\overrightarrow{grad}(T)\right) + S_v \quad (6)$$

where ρ is the density, C_p is an equivalent specific heat, that equals Cp in the cathode and arc-plasma domains, and is modified to $C_p + L_f\,\frac{df_L}{dT}$ in the anode domain to account for the latent heat of fusion L_f, k is the thermal conductivity, T is the temperature, and S_v is a volumetric heat source term.

In the plasma, this source term is expressed as follows:

$$S_v = S_J + S_{rad} = \vec{j}.\vec{E} - 4\pi\varepsilon_N \quad (7)$$

where S_J is the heating Joule effect (with j is current density, and E is electric field), and S_{rad} is the radiation losses with ε_N the emission coefficient of Argon.

Inside the cathode and the anode, the heat source term is only the heating Joule effect.

The electromagnetic force and the Joule heating are obtained from the resolution of electromagnetic equations:

$$\begin{gathered} div\left(\sigma_e \overrightarrow{grad}(V) + \sigma_e \frac{\partial \vec{A}}{\partial t}\right) = 0 \\ \sigma_e \frac{\partial \vec{A}}{\partial t} + \frac{1}{\mu_0} \overrightarrow{rot}\left(\overrightarrow{rot}\left(\vec{A}\right)\right) + \sigma_e \overrightarrow{grad}(V) = \vec{0} \end{gathered} \tag{8}$$

where σ_e is the electrical conductivity, V is the electrical potential, μ_0 is the magnetic permeability and A is the magnetic vector potential.

At the cathode/plasma interface, specific phenomena must be taken into account in the energy balance such as cathode ion neutralization, thermionic emission, and radiation losses from the cathode surface. This energy balance is formulated as follows [2]:

$$\vec{q}_c.(-\vec{n}) = \vec{q}_{pl}.(-\vec{n}) + q_{ions} + q_{thermionic} + q_{radiation} \tag{9}$$

where:

- $\vec{q}_c = -k_c \overrightarrow{grad}(T_c)$ with k_c is the cathode thermal conductivity and T_c is the temperature field in the cathode
- $\vec{q}_{pl} = -k_{pl} \overrightarrow{grad}(T_{pl})$ with k_{pl} is the plasma thermal conductivity and T_c is the temperature field in the plasma
- $q_{ions} = j_i V_i$ with j_i is the ion current and V_i is the gas ionisation potential
- $q_{thermionic} = -j_e \phi_c$ with j_e is the electron current and ϕ_c is the cathode work function
- $q_{radiation} = -\varepsilon \sigma_B T^4$ with ε is the anode emissivity, σ_B is the Stefan-Boltzmann constant and T is the temperature at the interface.

As for the cathode / plasma interface, specific phenomena must be taken into account in the energy balance such as the absorption of electrons by the anode, and the radiatio
n losses. This energy balance is expressed, according to Tanaka et al. [2], as follows:

$$\vec{q}_a.(-\vec{n}) = \vec{q}_{pl}.(-\vec{n}) + q_{electrons,condensation} + q_{radiation} \tag{10}$$

where:

- $\vec{q}_a = -k_a \overrightarrow{grad}(T_a)$ with k_a is the anode thermal conductivity and T_a is the temperature field in the anode,
- $\vec{q}_{pl} = -k_{pl} \overrightarrow{grad}(T_{pl})$ with k_{pl} is the plasma thermal conductivity and T_{pl} is the temperature field in the plasma,
- $q_{electrons,condensation} = |\vec{j}.\vec{n}|\phi_a$ with $|\vec{j}.\vec{n}|$ is the normal current density and ϕ_a is the anode work function,
- $q_{radiation} = -\varepsilon \sigma_B T^4$ with ε is the anode emissivity, σ_B is the Stefan-Boltzmann constant and T is the temperature at the interface.

Since the anode surface is considered as non-deformable, only drag force induced by the plasma jet on the melt pool surface and Marangoni effect are taken into account at the anode surface and can be formulated as follows:

$$F_{anode} = F_{shear} + F_{marangoni} \quad (11)$$

where:

- $F_{shear} = \left(\bar{\bar{\tau}} - P_{pl}\bar{\bar{I}}\right).\vec{n}).\vec{t}$ with $\bar{\bar{\tau}}$ the shear stress tensor, P_{pl} the plasma pressure applied to the top surface of the melt pool and $\vec{t}$ the tangential vector at the top surface of the melt pool.
- $F_{marangoni} = f_L \frac{\partial \gamma}{\partial T}\frac{\partial T}{\partial r}$ with γ the surface tension coefficient. With the introduction of the liquid fraction f_L in this expression, Marangoni force becomes zero at the anode surface in the solid phase.

VALIDATION OF THE MODEL

The aim of this section is to compare the results calculated by our model to those available in the literature. As mentioned previously, two reference cases have been used: Hsu [1] and Tanaka et al [3]. In [2], a copper anode cooled with water is considered, so the anode stays at the solid state. This reference case is used to compare the calculated results in the plasma. In particular, comparisons will focus on:

- Arc-plasma temperature
- The evolution of axial velocity in the arc column along the axis of symmetry.

In the second reference case [3], the anode is composed of stainless steel, which is heated by the arc until a melt pool is created. For this configuration, the shape of the weld pool, the shear forces applied to the melt pool surface, the heat flux as well as the current density at the surface of the anode are analysed and compared to the literature data.

All these results have been obtained with a computational domain meshed using standard Lagrangian quadratic triangular elements. The mesh size densities are as follows 8.10^{-4} m in the plasma, 5.10^{-5} m in melt pool domains, and 1.10^{-4} m in the cathode domain, 1.10^{-5} m at the top surface of the weld pool and the cathode, where high thermal gradients occur. Computations are performed within 1 hour on 8 processors computer (3.47GHz and 96 GB RAM DDR3) for a stationary calculation and 12 hours for a unsteady calculation.

Before presenting the results of our numerical models and in order to have a better analysis of the results, Table 1 summarizes the main differences between the different models of the literature as well as with our numerical model.

Table 1 Comparisons of assumptions used by the different authors [1], [4], [5], [6], [7]

	Brochard	**Traidia**	**Lago**	**Hsu**	**Tanaka**	**Our model**
Software	Cast3m	Comsol	FIUENT	Not specified	SIMPLEC	Comsol
Configurations	2D axisymmetric / Stationary	2D axisymmetric / Stationary	2D axisymmetric / Stationary	2D axisymmetric / Stationary	2D axisymmetric / Time-dependent	2D axisymmetric / Time-dependant
Assumptions						
Plasma	LTE	LTE	LTE	LTE	LTE	LTE
Plasma : Fluid	Incompressible	Incompressible	Weakly compressible	Not specified	Weakly compressible	Weakly compressible
Fluid flow	Laminar	Laminar	Laminar	Laminar	Laminar	Laminar
Anode surface	Not deformable	Not deformable	Not deformable	Not deformable	Not deformable	Not deformable
Cathode	Present	Present	Not present	Not present	Present	Present
Electromagnetic calculation	Method of least squares	Magnetic approach	Potential approach and magnetic approach	Magnetic approach	Not specified	General approach
Normal current density at the surface	$j = \frac{I}{\pi R_c^2}$	$j = \frac{I}{\pi R_c^2}$	$j(r) = J_{max}\exp(-br$ $J_{max} = \frac{I}{\pi R_c^2}$	$j(r) = J_{max}\exp(-br$ $J_{max} = \frac{I}{\pi R_c^2}$	$j(r) = J_{max}\exp(-br$ $J_{max} = \frac{I}{\pi R_c^2}$	$j(r) = J_{max}\exp(-br$ $J_{max} = \frac{I}{\pi R_c^2}$

One of the strongly criticisable assumptions is the normal current density applied. Indeed, it is virtually impossible to measure the plasma temperature as well as the electric field exactly near the tip of the cathode. It is therefore necessary to choose a reasonable pro of the current as Hsu formulated [1]:

$$j(r) = J_{max}\exp(-br) \tag{12}$$

Therefore, we have chosen to apply this same profile in our model. However, the constant b of equation (12) is determined using the equation (13):

$$I = \int_{\partial\Omega} -\vec{n}.\vec{j}\, dS = 2\pi \int_0^{R_c} j(r) r\, dr \tag{13}$$

Configuration of Hsu

In this configuration of Hsu [2], a thoriated tungsten cathode is used, with a copper anode and argon as a shielding gas. The arc current is fixed to I = 200A, the electrode-tip has an angle of 60° with a truncation radius of 0.3 mm, and the inter-electrode distance (arc length) is set to 10 mm. Many authors have reproduced this configuration like Brochard [5], Traidia [6], and Lago[7]. The material properties are temperature-dependant. The values of the properties and other parameters are given in these references.

Fig. 2 shows a comparison of the isotherms in the plasma calculated by our model and given by other authors [6], [7], [5], [1]

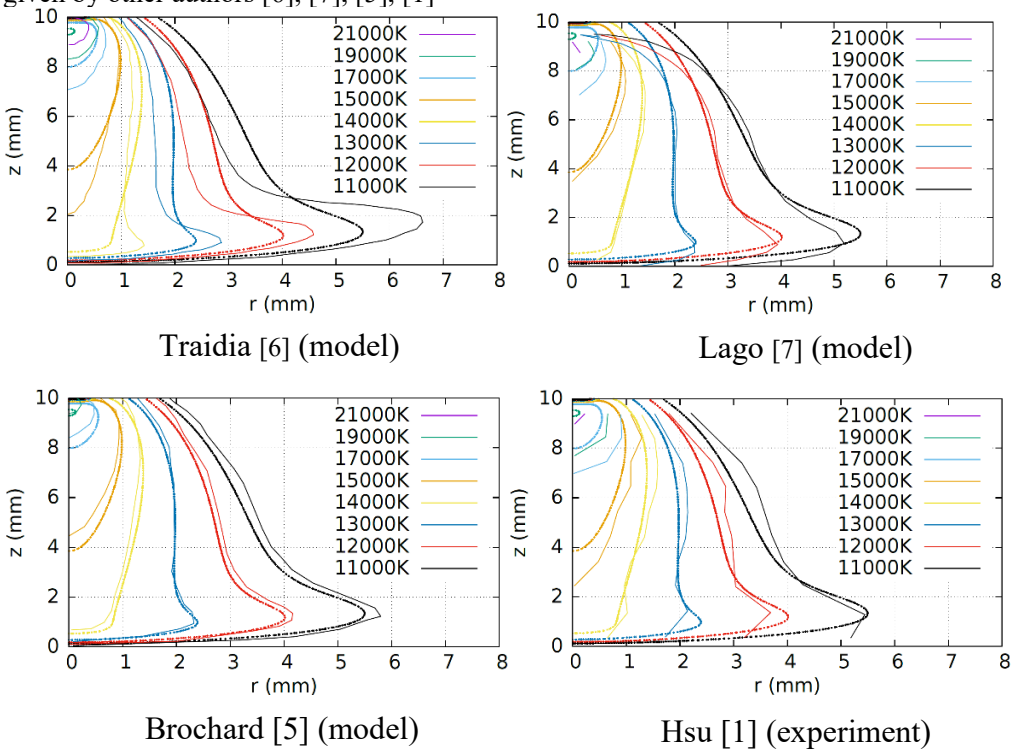

Fig. 2 Comparisons of isotherms of a free-burning between authors (dashed lines) and our model (continuous lines).

It can be observed that our model gives temperatures consistent with the numerical results of Traidia, Lago and Brochard and also the experimental data of Hsu. The differences between authors are relatively minor, in the range of several hundred kelvins. Nevertheless, the Lago's model lacks precision near the cathode. This shows that it is essential to take into account the cathode to predict the temperature field in this zone. However, the temperature field near the anode gives satisfactory results. The Traidia's model has wider isotherms than our model. One of its assumptions is the incompressible fluid flow in plasma. To highlight the effect of this assumption, a calculation with an incompressible fluid flow in our model was realized. The Fig. 3 shows that this assumption is too penalizing.

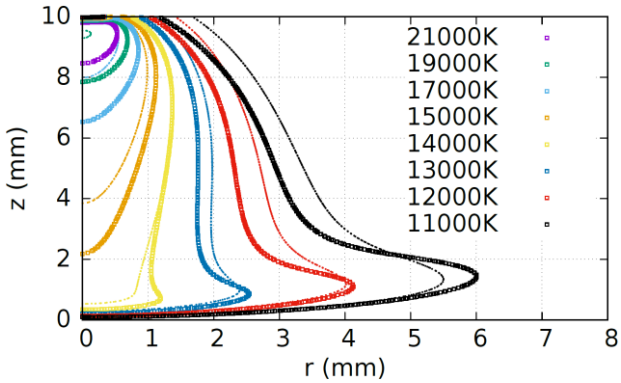

Fig. 3 Comparisons of isotherms of a free-burning between our model with an incompressible fluid flow (square lines) in plasma and with a weakly compressible fluid flow (dashed lines).

The Fig. 4 gives a comparison of the flow velocity along the axis of symmetry calculated by our model and the model of [1], [7], [5].

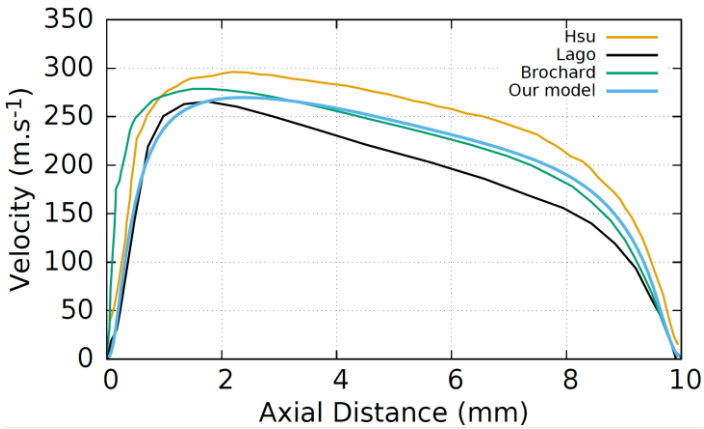

Fig. 4 Comparisons of flow velocity along the axis of the arc calculated by [1], [7], [5] and our model.

From Fig. 4, it can be observed that our model gives results consistent with the models of Hsu, Lago and Brochard. The flow velocities calculated by our model are close to the average velocities given by the different authors.

These comparisons show that our model gives consistent values for temperature and velocity in the plasma.

Configuration of Tanaka

In the configuration of Tanaka [3], a thoriated tungsten cathode is used with a 304 stainless steel anode and argon as a shielding gas. The arc current is fixed to I = 150 A, the electrode-tip has an angle of 60° with a truncation radius of 0.3 mm, and the inter-electrode distance (arc length) is set to 5 mm [2],[4]. Many authors are reproduced this study like Brochard

[5], Traidia [6]. The description of the model and all data used for this configuration are detailed in these references. The advantage of this second configuration is that it enables to validate the calculated temperatures and velocities in the melt pool.

The Fig. 5 shows the temperature field and velocity vectors in the whole geometry Fig. 5a) and in the melt pool (Fig. 5b). In the plasma, the order of magnitude of temperatures and velocities is consistent with the previous study. In the melt pool, the fluid flow velocity is also consistent with the Brochard's results. Brochard obtained a velocity of 0.31m/s and our model gives a velocity of 0.34 m/s.

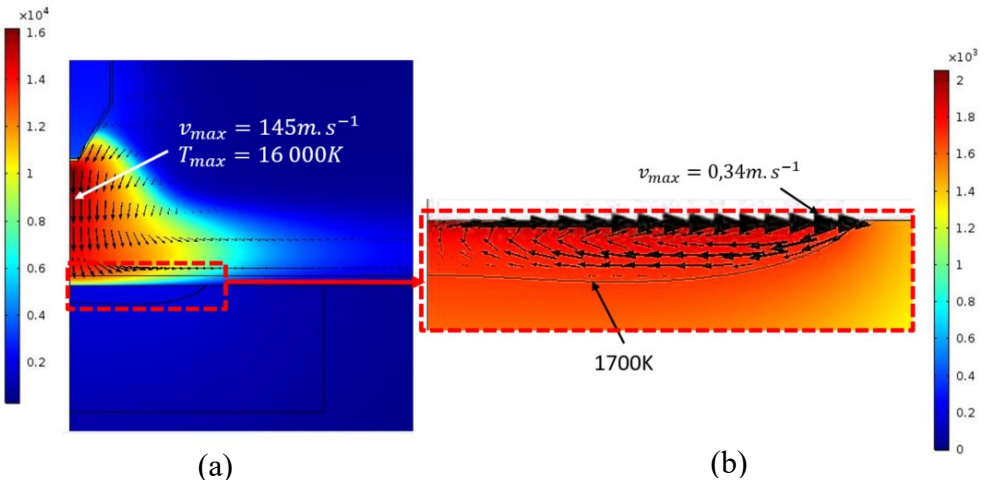

Fig. 5 Temperature field (K) and velocity vector in the whole geometry (a) as well as in the melt pool (b).

The results calculated by our model is compared to those given by Tanaka [2] [3], Brochard [5], and Traidia [6], in terms of :

- shear stress at the anode surface,
- current density at the anode surface,
- heat flux density at the anode surface,
- temperature at the anode surface.

The results can be seen in Fig. 6. Note that some authors do not present all these values. So our model is compared only with the available data presented in the literature.

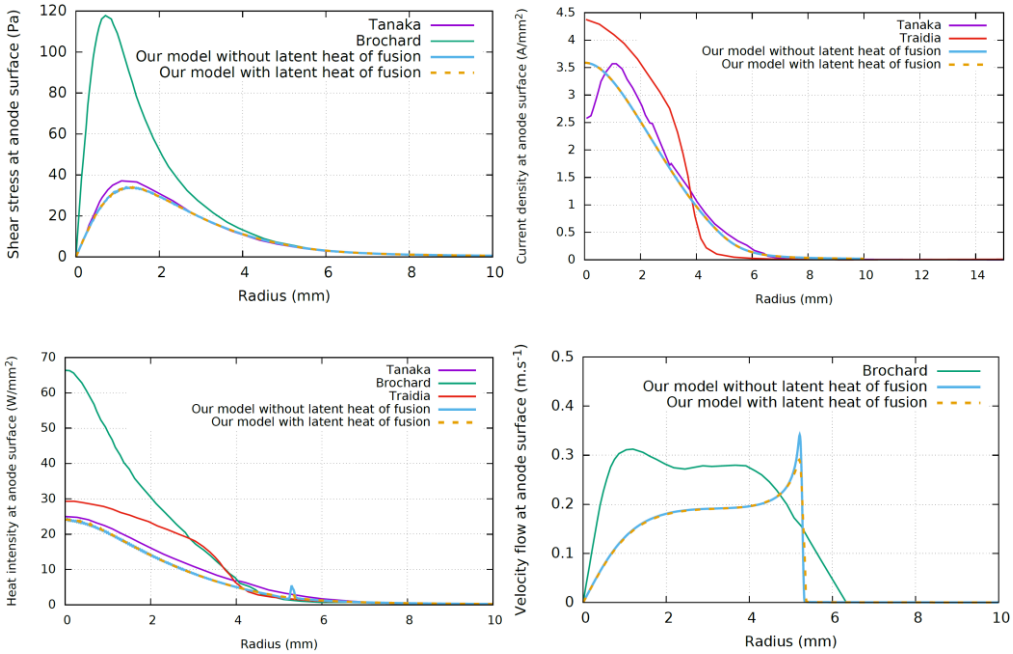

Fig. 6 Comparisons of shear stress, current density, heat intensity, and velocity flow at the surface of anode between authors and our model [2], [3], [5], [6].

These comparisons show that our model is overall consistent with the different authors. Only, Brochard has different results regarding shear stress and heat intensity at the anode surface. It is difficult to explain why Brochard obtained such discrepancies with other models of literature and our model. Note that such models are relatively complex and the authors do not give all the details of their model. Some material properties are not clearly indicated. The numerical methods used to solve the equations can differ. Different softwares are employed. The physics near the electrodes are very complicated due to the non Local Thermodynamic Equilibrium. The authors do not used the same method to treat the interfaces, as detailed in [8]. The arc initiation is also a delicate issue to simulate in such models. In order to further validate the model, the shape of the melt pool is compared with results given by [2], [5] (Fig. 7).

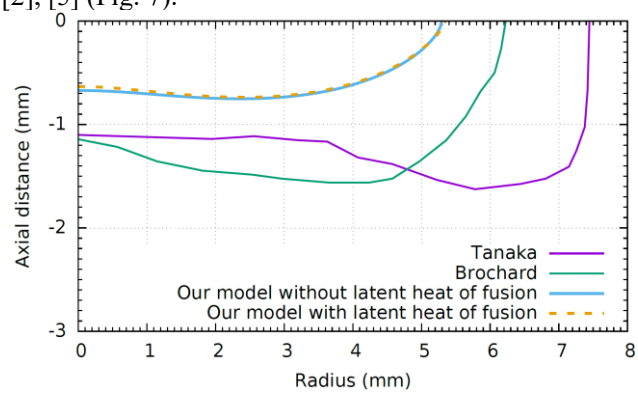

Fig. 7 Comparisons of shape of melt pool between authors and our model [2], [5].

Fig. 7 shows significant differences in the melt pool shapes calculated by the different authors. Tanaka and Brochard predict the same penetration depth but the melt pool width is larger for Tanaka. The global shape differs also. Our model predicts a smaller melt pool. Brochard obtained a larger melt pool than Tanaka and our model. From Fig. 6, it is possible to observe that the shear stress calculated by Brochard is higher than that given by our model, this could explain why our melt pool is narrower. However, it is more difficult to give an explanation for the difference observed for our model and Tanaka, since the results presented in Fig. 5 are very close between Tanaka and our model. One possible explanation could come from a different thermal boundary condition at the bottom of the anode. In order to better understand the observed differences, experiments will be planned in the future.

With regard to the latent heat of fusion, the Fig.6 and Fig. 7 shows that it has a very small influence on the results. Consequently, can be neglected in a stationary approach.

This first section enables to validate the model of arc welding. This model can be used to define boundary conditions for a model restricted to the melt pool. It provides the net heat flux, electromagnetic forces and shear stress caused by the drag force of arc at the melt pool surface as a function of only operating parameters such as arc length, electrode shape, or electrical current. Nevertheless, this model must be modified in order to represent a GMA process (or a WAAM process) in which the electrode is consumable. The melting of the anode creates droplets. The presence of these droplets in the plasma and their fall modify also the physical phenomena in the plasma. The boundary conditions for the electrical problem are also different since the electrons move in the opposite direction. The complete modelling of all these unsteady phenomena is more complex than the GTA modelling and a simplified approach is proposed in the next section. Indeed, the WAAM process is well adapted for the manufacturing of large parts. However, numerical models need to be simplify to reduce computational time for large geometries.

MODELING OF THE BUILDING OF THE ROD

In this section, a numerical model of wire arc additive manufacturing (WAAM) is presented. The aim is to build a rod along the vertical axis. This shape has the advantage to be simulated with a 2D axial-symmetry model in order to reduce computation time.

EXPERIMENTAL PROCEDURES

The definition and validation of the model are based on experimental data obtained by the Jean Rouxel Institute of Materials at University of Nantes (IMN) in France. In arc processes, various modes of metal transfer exist depending on many operating variables such as the arc current. Here, a pulsed metal inert gas (MIG) process is chosen. During this process, one droplet per pulse is created at the electrode tip with a detachment frequency of 25 Hz. The droplets then travel the arc plasma and fall into the melt pool. To build the rod, a first series of droplets are deposited on a cylindrical substrate of 12,7 mm diameter and 40 mm of height composed of 304 stainless steel. The wire is 308LSi stainless steel, its

diameter is 1 mm and is speed is 2 mm/min. The shielding gas is Argon, and the flow is 14 L/min. The distance between the nozzle and the cylindrical substrate is 12 mm. The arc height is fixed at 2 mm during one layer. One layer is composed of 62 droplets. The next layer is created when the temperature is below 300°C. This temperature is measured by an infrared camera.

During the process, a high-speed camera is also used to measure the diameter of the droplets and to obtain the evolution of the geometry of the layers.

The Fig. 8 illustrates the different rods obtained by additive manufacturing.

Fig. 8 Photographies of different rods by additive manufacturing.

The post mortem observables are obtained using a 3D scan that gives the final geometry of the piece, and by realizing macrographs to obtain the melted zone.

PRESENTATION OF THE MODEL

The developed model simulates the heating of the substrate by the arc, the falling of droplets in the melt pool and the solidification of the layer after arc extinguishes. To simplify the model, the droplet formation and detachment are not simulated. Indeed, the droplet enters at the top of the computation domain with a given size, velocity and temperature based on experimental data. The creation of the arc is also not integrated in this model, but the arc model presented in the previous section is used to define a heat source term applied at the free surface of the liquid phase. Note that this heat source terms needs to be adapted for a WAAM process. Lorentz forces, shear stress at the melt pool surface and Marangoni effect are also omitted in this first model in order to reduce computational time. An experimental validation will enable to discuss theses strong assumptions. The Fig. 9 illustrates the main steps of this simplified model.

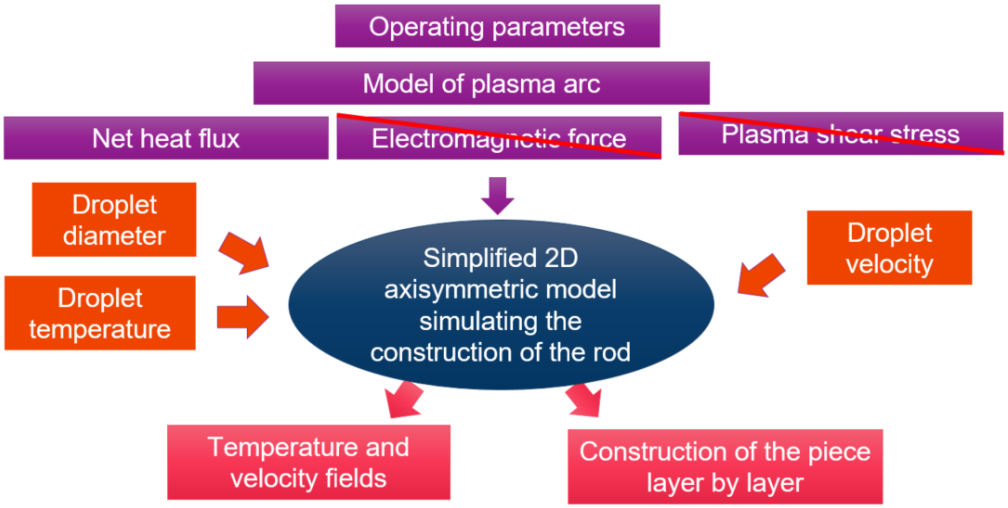

Fig. 9 Schematic diagram of the simplified approach for WAAM process.

Given the assumptions used for this model, only heat transfer and fluid flow are considered. The impingement of molten metal droplets into the melt pool and the resulting change in the melt pool shape are simulated using the level set method. This method is described in the next section.

PRESENTATION OF THE LEVEL SET METHOD

The level set method [22] consists in defining a ϕ variable on a fixed Cartesian grid to represent the interface between gas and metal. This variable ϕ is defined to 0 in gas, and 1 in metal. The interface is identified by the isovalue ϕ = 0.5. This variable also serves for defining the appropriate properties in each material (gas or metal). So, for example, the density is defined as follows:

$$\rho = \rho_{gas} + (\rho_{steel} - \rho_{gas})\phi \tag{14}$$

where ρ_{gas} represents the gas density and ρ_{steel} the metal density. These properties can be temperature-dependant. Note that, at the interface, a mean value for the material properties is set. At the vicinity of the gas/metal interface, a continuous variation in properties is modelled using a smooth step function (Fig. 10). However, the thickness of this transition must be small enough to represent the interface accurately but not too small, in order to avoid numerical convergence problems.

Once the variable is correctly defined, the interface is usually determined by simply locating the variable $\phi = 0.5$. The displacement of the interface is obtained by solving a transport equation related to the velocity of the fluids. The transport equation used is:

$$\frac{\partial \phi}{\partial t} + \vec{v}.\overrightarrow{grad}(\phi) = \gamma_{ls}\,\overrightarrow{div}\left(\varepsilon_{ls}\,\overrightarrow{grad}(\phi) - \phi(1-\phi)\frac{\overrightarrow{grad}(\phi)}{|\overrightarrow{grad}(\phi)|}\right) \tag{15}$$

where γ_{ls} is the reinitialization parameter and ε_{ls} is the interface thickness controlling parameter.

Moreover, the ϕ variable is also used to define a Dirac function $\delta(\phi)$. This function makes it possible to apply all the existing boundary conditions between the two fluids in the computational domain through source terms introduced into the conservation equations.

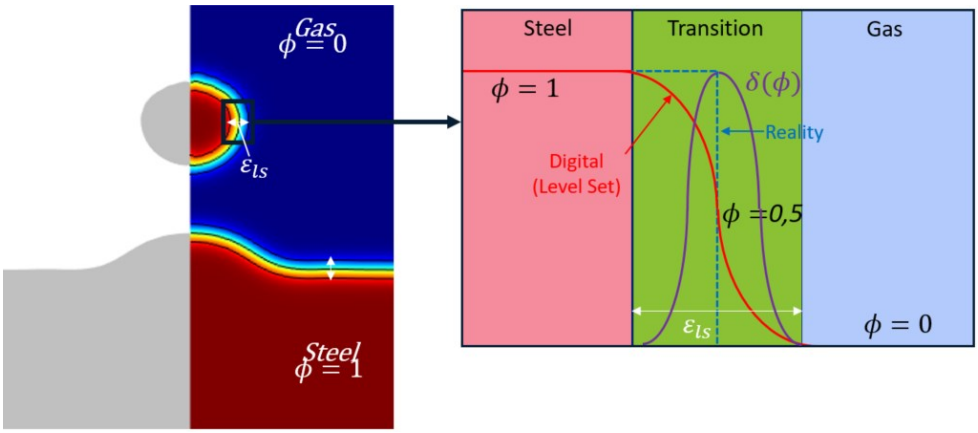

Fig. 10 Schematic drawing illustrating the level set method and the evolution of the $\boldsymbol{\phi}$ variable and Dirac function along the interface.

PRESENTATION OF THE EQUATIONS

In addition to the previously mentioned assumptions, the plasma and liquid metal are supposed to be incompressible Newtonian fluids in a laminar flow.

With these assumptions, the governing equations of heat and mass transfer for plasma and metal transport are given below:

- Conservation of mass

$$div(\vec{v}) = 0 \tag{16}$$

- Conservation of momentum

$$\rho\left(\frac{\partial \vec{v}}{\partial t} + \overline{\overline{grad}}(\vec{v}).\vec{v}\right) = \overrightarrow{div}\left[-P\bar{\bar{I}} + \mu_f\left(\overline{\overline{grad}}(\vec{v}) + {}^t\overline{\overline{grad}}(\vec{v})\right) - \frac{2}{3}div(\vec{v})\bar{\bar{I}}\right] + \overrightarrow{F_v} \tag{17}$$

The term source of momentum equation is expressed as follows:

$$\vec{F}_v = \vec{F}_g + \vec{F}_{Darcy} \times (\phi > 0{,}5) + \vec{F}_{st} = \rho\vec{g} + \left(-C\frac{(1-f_L)^2}{f_L^3 + b}\vec{v}\right) \times (\phi > 0{,}5) + div\left(\gamma\left(\bar{\bar{I}} - (\vec{n}.\vec{n}^T)\right)\delta(\phi)\right) \quad (18)$$

The Darcy law is necessary only for steel, because it is the only material to have a solid and liquid phase.

Conservation of Energy

$$\rho C_p\left(\frac{\partial T}{\partial t} + \vec{v}.\overrightarrow{grad}(T)\right) = div\left(\bar{\bar{\lambda}}\,\overrightarrow{grad}(T)\right) + S_v \times \delta(\phi) \quad (19)$$

The source term of energy is:

$$S_v = S_{NetHeatFlux} \times \delta(\phi) \quad (20)$$

where $S_{NetHeatFlux}$ is calculated by the model of arc and corresponds to the net heat flux at the melt pool surface (Fig. 11).

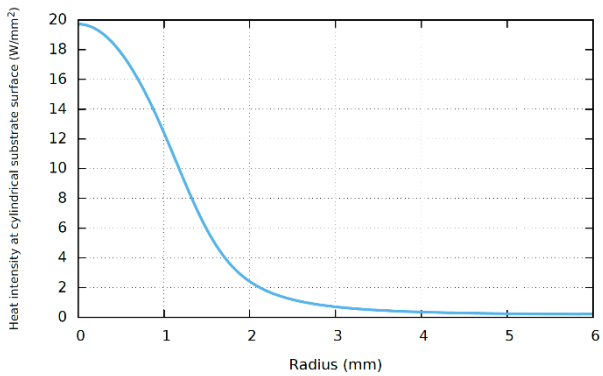

Fig. 11 The net heat flux at the melt pool surface ($\boldsymbol{S_{NetHeatFlux}}$).

The droplets are introduced at the top of the computation domain with an initial diameter D_d dependent on the wire electrode feed rate v_w and radius r_w, and the droplet detachment frequency f_d according to the following equation [10]:

$$D_d = \left(6r_w^2\frac{\rho_w}{\rho_d}\frac{v_w}{f_d}\right)^{1/3} \quad (21)$$

where ρ_w and ρ_d are the density of the wire and the droplet, respectively.

The diameter obtained by the equation (21) is 1.26 mm with the experimental parameters. Moreover, using the high speed camera, it is possible to measure the diameter of the droplet which is 1.27 mm. Consequently, the equation (21) gives a good estimation of the diameter of the droplet.

It was not possible to measure the temperature of the droplet with the used infrared camera since it is limited to 1500°C. The value of the droplet temperature is based on

literature data which is 2100 K [23]. The velocity of the droplet is obtained from the high speed camera. Its velocity is 0.063 m/s.

The material properties used in our calculations are given in Table 2.

Table 2 Material properties of 304 stainless steel and shielding gas used in our calculations.

	304 stainless steel	Gas
Thermal conductivity (W/m/K)	$k(T)$ [24]	0.08
Specific heat (J/kg/K)	$C_p(T)$ [24]	510
Density (kg/m^3)	6725	1
Dynamic Viscosity (Pa.s)	1.10^{-3}	0.1

The Fig. 12 illustrates the computation domain in order to simulate the building of the rod with different layers.

The computational domain is meshed using standard Lagrangian quadratic elements. The mesh size density is 5.10^{-5} m in all domains. Computations are performed within a day on 8 processors computer.

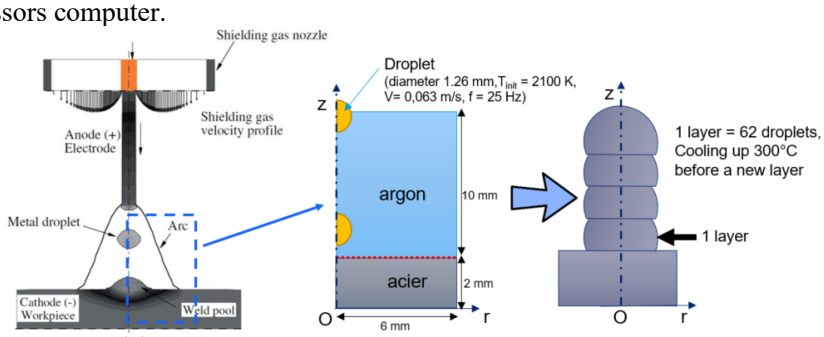

Fig. 12 (a) Schematic representation of a GMAW system [14], (b) Initial computation domain, (c) Schematic representation of the rod building.

RESULTS AND DISCUSSIONS

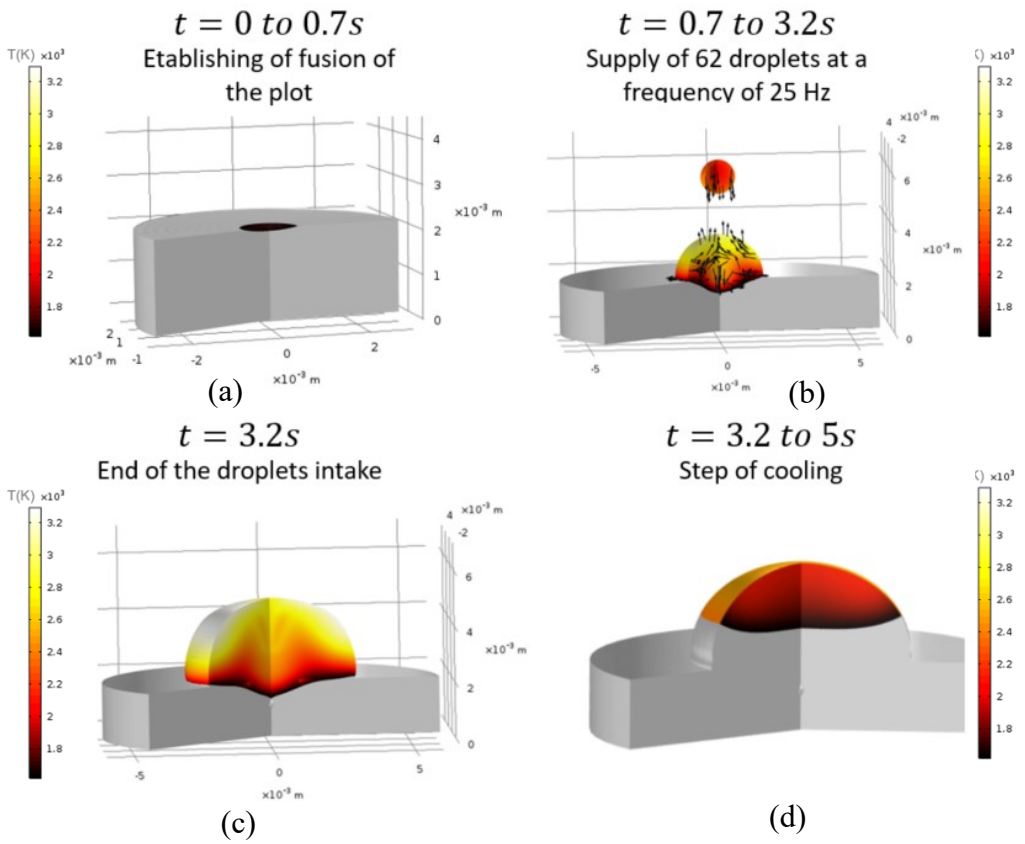

Fig. 13 Shape and temperature field at different times during the building of the first layer.

The Fig. 13 shows the shape of the rod and temperature field at different times during the building of the first layer. The cylindrical substrate is first heated during 0.7 s (Fig. 13a), then droplets are introduced at the top of the computation domain along the z-axis up to 3.2 s. Fig. 13c shows the temperature field and the shape of the first layer before cooling. Note that these figures are presented in 3D geometry during the post-processing procedure, but the calculations are performed in a 2D axial-symmetry geometry. At present, only the first layer has been simulated. The calculated shape of the first layer obtained after cooling is compared to the macrograph in Fig. 14. There is an error of about 8% in terms of volume. Therefore, there is a good agreement between experiment and model despite the strong assumptions.

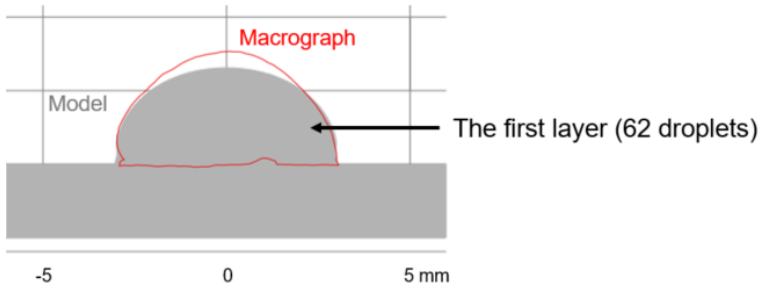

Fig. 14 Comparison of experimental (red) and numerical first layer.

Comparisons between the model and the experimental data are to be continued. The next steps will be to analyse the videos from the fast and thermal cameras, but also to simulate several layers and compare them to the experiments. Moreover, the model must be improved. Simplifying assumptions are to be discussed (electromagnetic forces, Marangoni, shear stress).

CONCLUSION

In this paper, a model of arc has been developed. It is able to calculate temperature, velocity and electromagnetic fields in the arc and the melt pool. The shape of the melt pool is also calculated from the operating parameters. This model has been used to define heat input for a WAAM model. The building of a cylindrical rod has been simulated. These first results have given satisfactory comparisons with experimental data.

In perspective, it is necessary to continue the comparison between the experiment and the model in terms of heat transfer. In addition, to keep the predictive side of the model, it is necessary to develop an arc model with a fuse electrode using operating parameters.

REFERENCES

[1] K. C. HSU, K. ETEMADI, AND E. PFENDER, 'Study of the free-burning high-intensity argon arc', *J. Appl. Phys.*, vol. 54, no. 3, pp. 1293–1301, Mar. 1983.

[2] M. TANAKA AND J. J. LOWKE, 'Predictions of weld pool profiles using plasma physics', *J. Phys. Appl. Phys.*, vol. 40, no. 1, pp. R1–R23, Jan. 2007.

[3] M. TANAKA, H. TERASAKI, M. USHIO, AND J. J. LOWKE, 'A unified numerical modeling of stationary tungsten-inert-gas welding process', *Metall. Mater. Trans. A*, vol. 33, no. 7, pp. 2043–2052, 2002.

[4] M. TANAKA, 'An introduction to physical phenomena in arc welding processes', *Weld. Int.*, vol. 18, no. 11, pp. 845–851, Nov. 2004.

[5] M. BROCHARD, 'Modèle physique et prédictif du procédé de soudage à l'arc TIG', Université de Provence, 2009.

[6] A. TRAIDIA, 'Multiphysics modelling and numerical simulation of GTA weld pools', Ecole Polytechnique, 2011.

[7] F. LAGO, J. J. GONZALEZ, P. FRETON, AND A. GLEIZES, 'A numerical modelling of an electric arc and its interaction with the anode: Part I. The two-dimensional model', *J. Phys. Appl. Phys.*, vol. 37, no. 6, pp. 883–897, Mar. 2004.

[8] L. LI, B. LI, L. LIU, AND Y. MOTOYAMA, 'Numerical Modeling of Fluid Flow, Heat Transfer and Arc–Melt Interaction in Tungsten Inert Gas Welding', *High Temp. Mater. Process.*, vol. 36, no. 4, Jan. 2017.

[9] X. YAU, 'Modélisation numérique instationnaire pour la simulation du soudage TIG avec couplage plasma / bain de fusion', Aix Marseille université, Marseille, 2018.

[10] A. B. MURPHY, 'Influence of droplets in gas–metal arc welding: new modelling approach, and application to welding of aluminium', *Sci. Technol. Weld. Join.*, vol. 18, no. 1, pp. 32–37, Jan. 2013.

[11] Y. LUO, J. LI, J. XU, L. ZHU, J. HAN, AND C. ZHANG, 'Influence of pulsed arc on the metal droplet deposited by projected transfer mode in wire-arc additive manufacturing', *J. Mater. Process. Technol.*, 2018.

[12] H. G. FAN AND R. KOVACEVIC, 'A unified model of transport phenomena in gas metal arc welding including electrode, arc plasma and molten pool', *J. Phys. Appl. Phys.*, vol. 37, no. 18, pp. 2531–2544, Sep. 2004.

[13] J. HU AND H. L. TSAI, 'Heat and mass transfer in gas metal arc welding. Part I: The arc', *Int. J. Heat Mass Transf.*, vol. 50, no. 5–6, pp. 833–846, Mar. 2007.

[14] J. HU AND H. L. TSAI, 'Heat and mass transfer in gas metal arc welding. Part II: The metal', *Int. J. Heat Mass Transf.*, vol. 50, no. 5–6, pp. 808–820, Mar. 2007.

[15] S. TANGUY AND A. BERLEMONT, 'Application of a level set method for simulation of droplet collisions', *Int. J. Multiph. Flow*, vol. 31, no. 9, pp. 1015–1035, Sep. 2005.

[16] O. DESMAISON, G. GUILLEMOT, AND M. BELLET, 'Numerical modelling of hybrid arc/laser welding: a coupled approach to weld bead formation and residual stresses', p. 12.

[17] X. BAI ET AL., 'Numerical analysis of heat transfer and fluid flow in multilayer deposition of PAW-based wire and arc additive manufacturing', *Int. J. Heat Mass Transf.*, vol. 124, pp. 504–516, Sep. 2018.

[18] F. HEJRIPOUR, D. T. VALENTINE, AND D. K. AIDUN, 'Study of mass transport in cold wire deposition for Wire Arc Additive Manufacturing', *Int. J. Heat Mass Transf.*, vol. 125, pp. 471–484, Oct. 2018.

[19] J. HAIDAR, 'Local thermodynamic equilibrium in the cathode region of a free burning arc in argon', *J. Phys. Appl. Phys.*, vol. 28, no. 12, p. 2494, 1995.

[20] J. MOUGENOT, J.-J. GONZALEZ, P. FRETON, AND M. MASQUÈRE, 'Plasma–weld pool interaction in tungsten inert-gas configuration', *J. Phys. Appl. Phys.*, vol. 46, no. 13, p. 135206, Apr. 2013.

[21] A. B. MURPHY, M. TANAKA, K. YAMAMOTO, S. TASHIRO, J. J. LOWKE, AND K. OSTRIKOV, 'Modelling of arc welding: The importance of including the arc plasma in the computational domain', *Vacuum*, vol. 85, no. 5, pp. 579–584, Nov. 2010.

[22] S. OSHER AND J. A. SETHIAN, 'Fronts propagating with curvature-dependent speed: Algorithms based on Hamilton-Jacobi formulations', *J. Comput. Phys.*, vol. 79, no. 1, pp. 12–49, Nov. 1988.

[23] X. ZHOU, H. ZHANG, G. WANG, AND X. BAI, 'Three-dimensional numerical simulation of arc and metal transport in arc welding based additive manufacturing', *Int. J. Heat Mass Transf.*, vol. 103, no. Supplement C, pp. 521–537, Dec. 2016.

[24] C. S. KIM, 'Thermophysical Properties of Stainless Steels', Argonne National Laboratory Ill (USA), ANL--75-55, 1975.